International Journal of Solids and Structures 51 (2014) 754–766

Contents lists available at ScienceDirect

International Journal of Solids and Structures

journal homepage: www.elsevier.com/locate/ijsolstr

Modeling dynamic brittle behavior of materials with circular flaws or pores

C.Z. Katcoff, L.L. Graham-Brady *

Dept. of Civil Engineering/Hopkins Extreme Materials Institute, Johns Hopkins University, Baltimore, MD 21218, USA

ARTICLE INFO

Article history:
Received 15 July 2013
Received in revised form 2 October 2013
Available online 18 November 2013

Keywords:
Strain-rate dependent strength,
Micromechanics
Damage mechanics
Brittle failure
Porous materials

ABSTRACT

Compressive failure of brittle materials is driven primarily by crack growth from pre-existing flaws in the material. These flaws, such as grain boundaries, pores, preexisting cracks, inclusions and missing grains, are randomly spaced and have a range of possible shapes and sizes. The current work proposes a micromechanics-based model for compressive dynamic failure of brittle materials with circular pore flaws, which incorporates both the number density and the size distribution of flaws. Results show that the distribution of flaw sizes is very important, particularly at moderate strain rate, since analyses based solely on the mean flaw size overpredict strength. Therefore, in order to increase dynamic strength at low to moderate strain rates, it is most effective to control the presence of large flaws. At very high strain rates, however, crack growth is activated even in small flaws and therefore controlling the total number density rather than the size of the flaws is effective for increasing dynamic strength. Finally, the model shows that neglecting very small flaws in the pore population may not have significant effects on the results in many cases, suggesting that the model is a useful tool for identifying a minimum resolution required for experimental characterization of microstructure.

1. Introduction

Brittle materials have many uses – from dishware, to concrete buildings, to personnel armor. Prediction of brittle material strength under static loading is fairly well understood; however, it is important to understand how these materials respond to high-rate (dynamic) loading. For example, protection from blast loading for concrete structures relies on the ability to understand how concrete responds to high-rate loading. Additionally, improvements in ceramic manufacturing have enabled lightweight and durable ceramic personnel armors that are capable of withstanding significant dynamic loads. In the current work, a two-dimensional mechanics-based model is applied to predict the mechanical response of brittle materials with circular void flaws under dynamic compressive loading. Circular flaws represent the voids and weak inclusions observed in many brittle materials, such as concrete, ceramics and rock.

To model porous materials, we start by creating a two dimensional damage-based model for a brittle material with circular void flaws. Budiansky and O'Connell (1976) proposed a basic damage model for homogenized crack growth in brittle materials with a population of randomly oriented cracks. Horii and Nemat-Nasser (1986) developed a damage model specifically for closed cracks with frictional sliding on the crack interface, which becomes equivalent to the Budiansky and O'Connell model if the cracks are open. Subsequent models have been developed for brittle materials under compression, assuming a uniform distribution of flaws (e.g., Ravichandran and Subhash, 1995; Huang et al., 2002; Deshpande and Evans, 2008). Many of these models do not account for a distribution of flaw sizes and/or orientations, nor do they all address the effects of interaction. Damage associated with flaws that surround a given flaw affects the local stress state on that particular flaw; therefore, this interaction is an important component of failure. Paliwal and Ramesh (2008) established a model for materials with slit-like flaws that accounts for a distribution of flaw sizes and flaw orientations. The model enables consideration of a flaw population with a distribution of flaw sizes, and crack interaction is addressed through a self-consistent model that considers the material damage. The basis of this micromechanical model is a mode of failure known as axial-splitting. In other words, the inclined slit flaws drive crack growth as the frictional sliding at the inclined interface leads to Mode I tensile stresses at the crack tip.

While we do not observe the same sort of sliding mechanism in pores, an axial splitting mode occurs that is associated with tensile hoop stresses that occur at the extrema of the pores in the compressive loading direction (on the top and bottom of the pores shown in Fig. 1). Because this axial splitting mode is common to both slit-like and pore-like flaws, we apply the Paliwal and Ramesh model (2008) to brittle materials with pore-like flaws in the current work. This

* Corresponding author. Tel.: +1 4105168167.
E-mail address: lori@jhu.edu (L.L. Graham-Brady).

0020-7683/$ - see front matter © 2013 Elsevier Ltd. All rights reserved.
http://dx.doi.org/10.1016/j.ijsolstr.2013.11.004

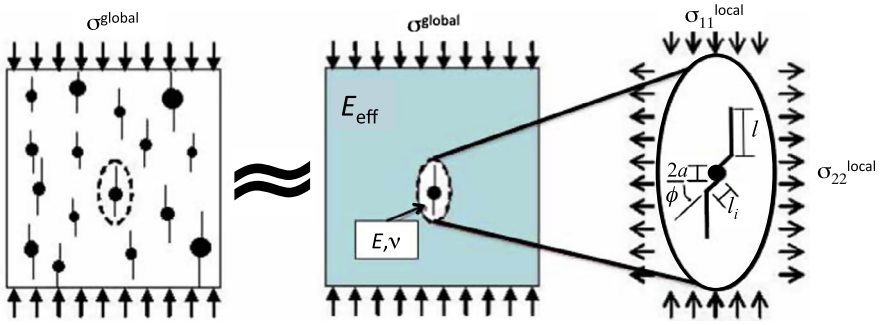

Fig. 1. Diagram of self-consistent model for a material with pore flaws. Local stresses σ^{local} are calculated based on elasticity solution to an elliptical inclusion in a damaged matrix under a far-field stress σ^{global}.

model is capable of incorporating the full range of pore sizes and the number density of pores into the calculations.

2. Model formulation

While the current model follows the general framework established in Paliwal and Ramesh (2008), the mechanics of crack growth associated with these pore-like flaws is quite different than the slit-like flaws. In order to highlight the similarities and differences between the models, each stage of the process is outlined in this section. Assuming a constant strain rate loading, the model steps through time using an explicit finite difference approach to calculate stress and damage at each time step.

The first task at a given time step is to calculate the state of stress acting on individual flaws, assuming the global stress and damage are equal to those calculated at the end of the previous time step. This is done through a self-consistent approach where each flaw is treated as a single flaw located within an elliptical inclusion of pristine material (see Fig. 1 for an overview of the self-consistent approach). Surrounding this inclusion, the remaining material is viewed as a damaged matrix material with anisotropic elastic properties, such as effective elastic moduli E_{eff}. These anisotropic elastic properties are calculated based on the global damage at the end of the previous time step. In an undamaged material, the local stress state is the same as the far-field stress state. However, with material damage, the elastic properties of the matrix degrade, causing an elastic mismatch at the matrix–inclusion boundary. This mismatch leads to a local stress state that differs from the far-field stress state. For example, with a damaged matrix material and far-field uniaxial compression, the self-consistent model predicts a tensile transverse local stress on the inclusion. This tensile stress is a significant contributor to crack growth, particularly when the material is highly damaged.

The second task at each time step is to use the local stress to calculate the Mode I stress intensity at the tip of the crack associated with each flaw. Sammis and Ashby (1986) derived a relationship for the stress intensity based on the exact solutions by Sih (1973):

$$K_I = \left[\frac{-1.1(1-2.1\lambda)}{(1+L)^{3.3}} + \lambda\right]\sigma_{11}\sqrt{\pi l}, \quad L \geqslant L_i \tag{1}$$

where σ_{11} is the compressive stress in the direction of the axial crack, λ is the ratio of transverse to axial stress (σ_{22}/σ_{11}), L is the ratio of the crack length to the pore radius (l/a, see the right-hand side figure in Fig. 1), and L_i is the normalized initial crack length (l_i/a). L is initially set equal to L_i. If $l = 0$ we note that the stress intensity is zero and cracks cannot initiate or grow. This necessitates the use of a 'pop-in' crack of length l_i, which Sammis and Ashby (1986) observed in experiments showing that cracks initially grow rapidly from circular holes but reach equilibrium as a small 'pop-in' length.

The idealized circular pore with initial cracks aligned perfectly in the direction of maximum compression is not likely in real materials. Pores and soft inclusions are not typically perfectly circular, and initial cracks are likely to follow surrounding grain boundaries or other defects that may be at an angle. For example, the microstructure in Fig. 2 suggests the use of modified pore flaws (in red), as illustrated in Fig. 3. In other words, we view each pore as a circular void with small initial inclined cracks at the locations of the largest tensile stresses.

For this modified pore, subsequent crack growth follows experimental observations of axial splitting, with growth parallel to the direction of maximum compression. In order to calculate the Mode I stress intensity at the crack tip of the modified pore, we add the stress intensity associated with two inclined initial cracks to the Sammis and Ashby (1986) stress intensity for pores (see Fig. 3). In particular, we add a term that accounts for the distance between the two slit flaws on either side of the pore using Horii and Nemat-Nasser (1986):

$$K_I = \left[\frac{-1.1(1-2.1\lambda)}{(1+L)^{3.3}} + \lambda\right]\sigma_{11}\sqrt{\pi l} + \frac{-(0.15 * a)\tau_{eff}\cos(\phi)}{\sqrt{\pi(l+a)}}\left[\sqrt{\frac{l+2a}{l}} + \sqrt{\frac{l}{l+2a}}\right] \tag{2}$$

where σ_{11}^{local} is the local axial compressive stress, λ is the ratio of transverse stress to axial stress ($\sigma_{22}^{local}/\sigma_{11}^{local}$), l_i is the inclined initial crack length, ϕ is orientation of the inclined initial crack (see Fig. 1), and τ_{eff} is the local effective sliding stress resolved on the inclined initial cracks (see Budiansky and O'Connell, 1976 for details). Minimizing Eq. (2) with respect to l shows that the minimum value of stress intensity corresponds to a crack length $l = 0.15a$. In other words, cracks smaller than $0.15a$ will exhibit unstable growth once initiated, until they reach $0.15a$. This occurs in a manner similar to 'pop-in' cracks observed in Sammis and Ashby's experiments (Sammis and Ashby, 1986). For this reason, $0.15a$ is used as the initial inclined crack length l_i.

The third task at each time step is to calculate the total damage Ω. For each pore radius a_j, the local stress intensity $K_{I,j}$ is calculated using Eq. (2). Cracks associated with a given pore radius a_j are assumed to grow when the crack tip stress intensity $K_{I,j}$ exceeds the Mode I fracture toughness of the material (K_{Ic}), with a crack growth rate:

$$\dot{l}_j = \frac{C_R}{\alpha}\left[\frac{K_{I,j} - K_{Ic}}{K_{I,j} - K_{Ic}/2}\right]^{\gamma} \tag{3}$$

where C_R is the material Rayleigh wave speed and α and γ are fitting parameters. The total crack length l_j is updated from this crack growth rate as:

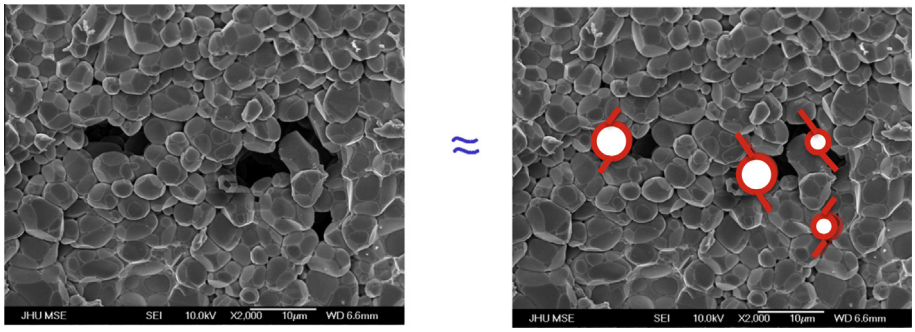

Fig. 2. AlN microstructure (Hu, 2012), which suggests a modified pore flaw to represent missing grains.

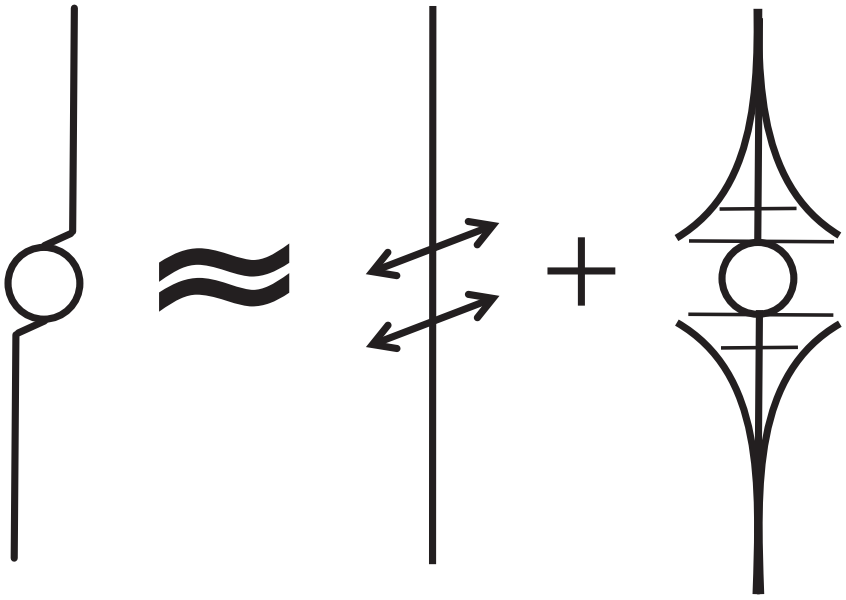

Fig. 3. Illustration showing the breakdown of stress intensity for the modified pore model.

$$l_j = l_j + \dot{l}_j \Delta t \tag{4}$$

The global damage is the sum of the squared crack length associated with every pore radius a_j, weighted by the number density of pores of that size (Paliwal and Ramesh, 2008):

$$\Omega = \eta \sum_{j=1}^{N} l_j^2 g(a_j) \Delta a \tag{5}$$

where η is two dimensional flaw density, and $g(a_j)$ is the discretized probability density function describing flaw radius a.

The final task at each time step is to update the anisotropic elastic properties and the global stress, based on the updated global damage Ω. Budiansky and O'Connell (1976) predict a damaged isotropic elastic modulus:

$$E_{eff} = E\left[1 - \frac{\pi^2}{30}(1 + \nu_{eff})(5 - 4\nu_{eff})\Omega\right] \tag{6}$$

where E is the undamaged elastic modulus of the material. In our study, because cracking is occurring in an axial splitting mode (see Fig. 1), we expect that the damage will reduce the modulus in the direction perpendicular to the loading (E_{2eff}) more than it will reduce the modulus in the direction parallel to the loading (E_{1eff}). Therefore, the elastic modulus in the two directions should differ. Here we assume that these two moduli are related by an anisotropy factor f:

$$\begin{aligned} E_{1eff} &= E\left[1 - \frac{\pi^2}{30}(1 + \nu)(5 - 4\nu)\Omega f\right] \\ E_{2eff} &= E\left[1 - \frac{\pi^2}{30}(1 + \nu)(5 - 4\nu)\Omega\right] \end{aligned} \tag{7}$$

where $0 \leqslant f \leqslant 1$. Increasing the length of wing cracks (l in Fig. 1) enables increased sliding at the flaw interface, and therefore axial splitting has an indirect effect on the damaged stiffness E_{1eff} in the loading direction. Because of this we assume f to be 0.3. In the absence of conclusive evidence suggesting otherwise, the Poisson's ratio is assumed to remain constant with damage ($\nu_{eff} = \nu$). The global stress is updated based on the effective elastic modulus E_{1eff}:

$$\begin{aligned} \dot{\sigma} &= E_{1eff}\dot{\varepsilon} + \dot{E}_{1eff}\varepsilon \\ \sigma^{global} &= \sigma^{global} + \dot{\sigma}\Delta t \end{aligned} \tag{8}$$

The updated global stress and damage are the initial conditions for the calculations at the next time step. The analysis continues until a maximum damage threshold is reached.

Table 1
Material properties assumed for model (based on AlN Hu, 2012).

Elastic Modulus, E	Poisson's ratio, ν	Mass density, ρ	Mode-I critical stress intensity, K_{Ic}	Cohesion, τ_c	Coefficient of friction, μ
320 GPa	0.237	3200 kg/m^3	2.8 MPa m	0	0.4

3. Numerical examples

In order to illustrate the effect of the parameters describing the flaw population on dynamic material strength, we consider three classes of flaw populations in our study: (1) a uniform flaw size; (2) a bi-valued flaw size; and, (3) a full flaw size distribution. The first class of flaw population allows us to isolate the effects of varying only flaw density, flaw size, and porosity. The second class of flaw population tells us the relative effects from two parts of the same flaw population: a large proportion of small flaws as opposed to a small proportion of large flaws. The third class of flaw population addresses the effects of the shape of the flaw size distribution and of neglecting small flaw sizes. In all of the examples presented here, we use the material properties for aluminum nitride (see Table 1). Other parameters used in the model are not well defined for aluminum nitride but are assumed to be the following for the purposes of this parametric study: the crack growth parameters α and γ are 1, the initial pop-in crack length is 15% of the pore flaw radius (see earlier discussion), and the initial pop-in orientation is 55.9° which is the angle at which the sliding forces are maximized given the coefficient of friction of 0.4 (Paliwal and Ramesh, 2008). Keeping these parameters constant allows the discussion to focus on the specific effects of flaw population on the dynamic stress–strain relationship.

In order to illustrate the various stages of damage that occur in a typical analysis, a sample stress–strain curve calculated from the model is shown in Fig. 4 for a material with 3.16×10^7/m^2 pores of radius 10 μm, under a uniaxial compressive strain rate of 10^6/s. At lower strain values, Fig. 4 shows elastic behavior with a linear stress–strain relationship. At higher strains, the flaws begin to initiate stable crack growth, which leads to an increase in damage. This increase in damage translates to a decrease in stiffness, so that the slope of the stress–strain curve decreases. When the peak stress is reached, defined here as the material strength, the slope of the curve becomes negative. This post-peak behavior is most readily associated with unstable crack growth and ultimately material failure. The sections that follow consider this stress–strain curve and the predicted strength for various flaw populations. We note that the predicted strength is high relative to actual material strengths, and the factors leading to this overprediction are outlined in the Discussion section following the numerical examples. At any rate, the results in Fig. 4 show that the model is capable of predicting crack-related damage growth for a given flaw population; therefore, we are confident that the predicted trends with respect to flaw population are reasonable.

3.1. Uniform flaw size

Assuming that all flaws are of uniform size, changes in predicted strength will be caused only by changes in density η, flaw radius a, and porosity ϕ, which are related as follows:

$$\phi = \eta \pi a^2 \tag{9}$$

Eq. (9) shows that only two of these three parameters are independent. In this example, we fix each of the three parameters and study the effect of varying the other two.

First, we set a fixed pore radius of 10 μm and increase the number of flaws per area (and therefore the porosity according to Eq. (9)). Assuming a strain rate of 10^3/s, Fig. 5 shows that increasing flaw density (and therefore porosity) decreases strength. Eqs. (2) and (3) show that flaws of the same size experience approximately the same crack growth rate at a given stress; therefore, increasing the flaw density increases the damage, since global damage $\Omega = \eta l^2$ scales linearly with flaw density η. This increased damage level translates to lower strength, justifying the result that an increase in flaw density decreases strength. At a higher strain rate of 10^6/s (shown in Fig. 6), the same trend with respect to flaw density is predicted. The predicted strength values are only slightly higher than the strengths predicted at lower rates, but the curvature of the stress–strain curve is quite different. At this loading rate, the pre- and post-peak curvature is much more pronounced, because the limits on crack growth speed (see Eq. (3)) are reached at this very high strain rate, which inhibits the rate of damage growth and therefore allows the stress to continue to grow at higher damage levels.

The predicted values of strength are summarized in Table 2 for multiple strain rates. An increase in flaw density (with a fixed flaw size) decreases the predicted strength at every strain rate. The

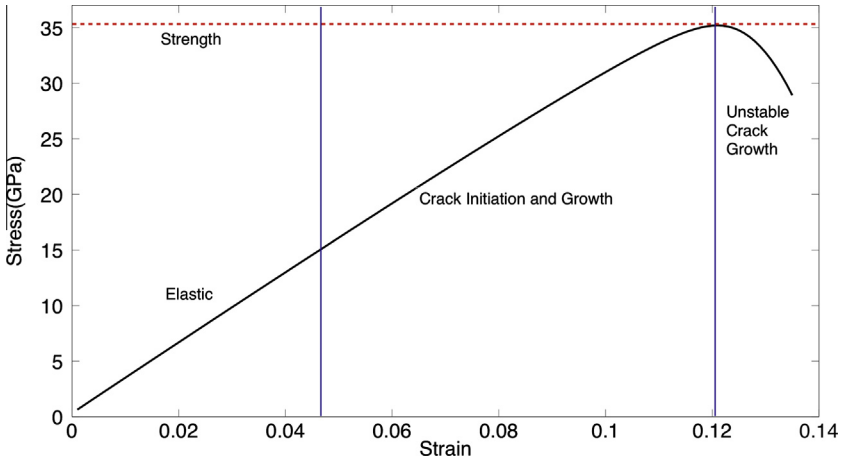

Fig. 4. Stress vs. strain for a microstructure with 3.16×10^7 pores/m^2, all of radius 10 μm, at a constant strain rate of 10^6/s.

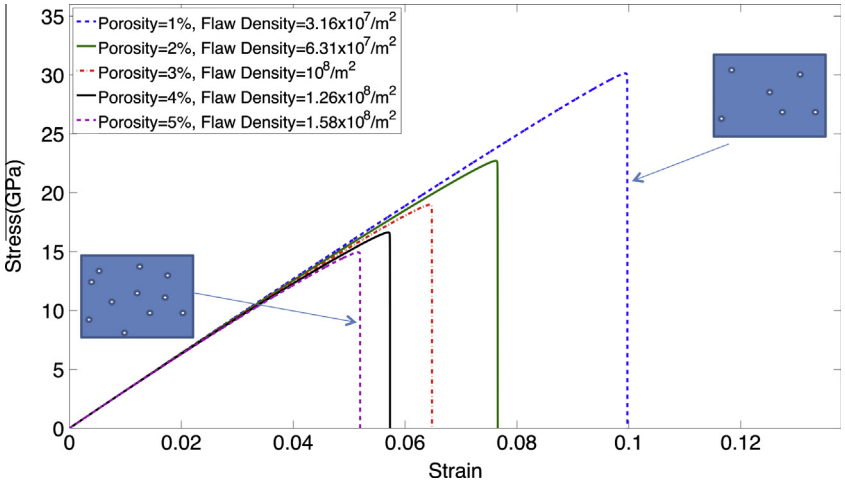

Fig. 5. Uniaxial compressive stress vs. strain at a constant strain rate of 10^3/s, for microstructures with 10 μm radius pores and an increasing porosity from 1% to 5%.

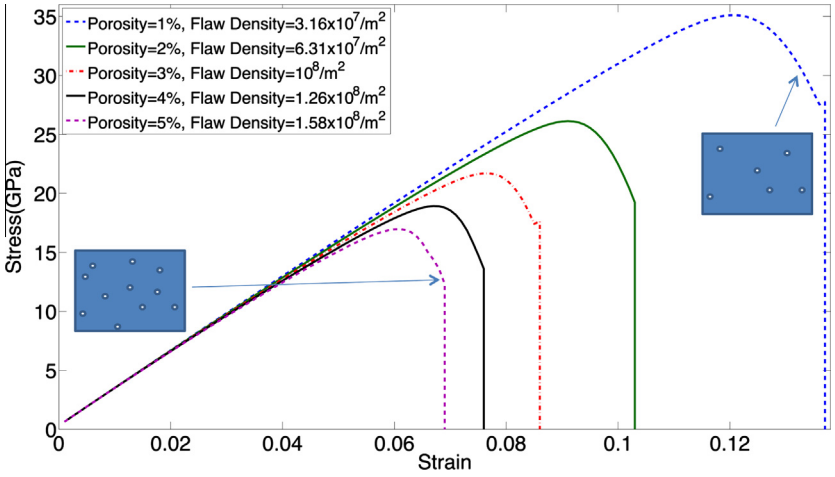

Fig. 6. Uniaxial compressive stress vs. strain at a constant strain rate of 10^6/s, for microstructures with 10 μm radius pores and an increasing porosity from 1% to 5%.

Table 2
Predicted uniaxial compressive strength for microstructure with equal sized pore flaws of radius 10 μm, at different strain rates and varying flaw densities.

Porosity (%)	Flaw density (/m^2)	Strength (GPa) at various strain rates/percentage increase from strength at strain rate 10^3/s			
		Strain rate = 10^3/s	Strain rate = 10^4/s (%)	Strain rate = 10^5/s (%)	Strain rate = 10^6/s (%)
1	3.16×10^7	30.1	30.2/0.3	30.9/2.7	35.1/16.6
2	6.31×10^7	22.7	22.7/0	23.2/2.2	26.1/15.0
3	10^8	19.0	19.0/0	19.4/2.1	21.7/14.2
4	1.26×10^8	16.6	16.6/0	17.0/2.4	18.9/13.9
5	1.58×10^8	14.9	14.9/0	15.2/2.0	17.0/14.1

small percentage increases in strength with strain rate are relatively constant from one flaw density to the next; therefore, the strain rate dependency is not strongly tied to flaw density.

Having seen the effect of flaw density on strength and strain rate dependency, we now fix the flaw density to 10^6/m^2 and vary the pore radius (and therefore the porosity). Fig. 7 shows the stress–strain curves for a uniaxial compressive strain rate of 10^3/s, with a uniform flaw radius increasing from 56 to 126 μm (corresponding to a range of 1% to 5% porosity). These results show that the higher porosity material, with the largest pores, has the lowest strength. Because larger pores exhibit higher stress intensities at the crack tip (see Eq. (2)), the crack growth speed is faster. This greater crack growth speed leads to higher damage, which decreases the overall strength of the material.

Fig. 8 shows the resulting stress–strain curves at a higher strain rate of 10^6/s. Similar to the results in Figs. 5 and 6, we see more curvature in the stress–strain curves at the higher strain rate. Comparing Figs. 7 and 8, there is a clear strain rate effect. The strengths predicted at the high strain rate are much less sensitive to pore radius than the strengths predicted at low strain rates. At the high strain rate, the limits on the crack growth speed are overcome by the very high rate of loading; therefore, the material is able to carry higher stresses before ultimate failure. In effect, the strength is driven by strain rate as much as by the damage growth rate.

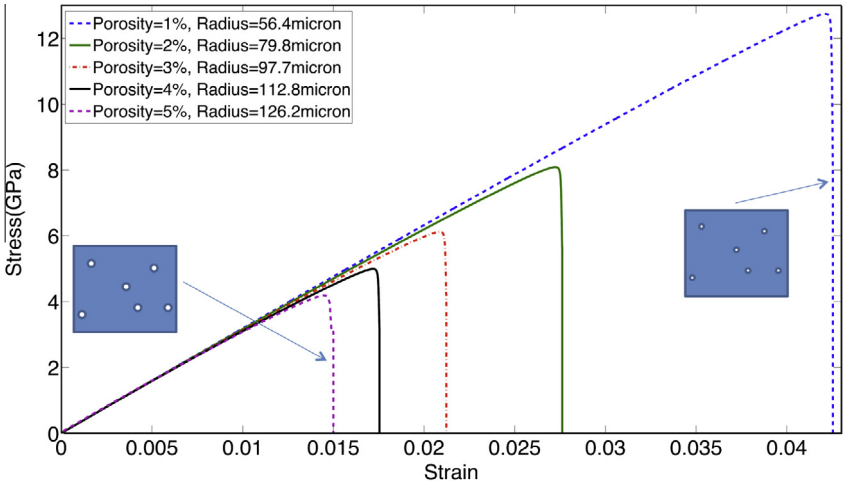

Fig. 7. Uniaxial compressive stress vs. strain at a constant strain rate of 10^3/s, for microstructures with 10^6/m^2 flaw density and an increasing porosity from 1% to 5%.

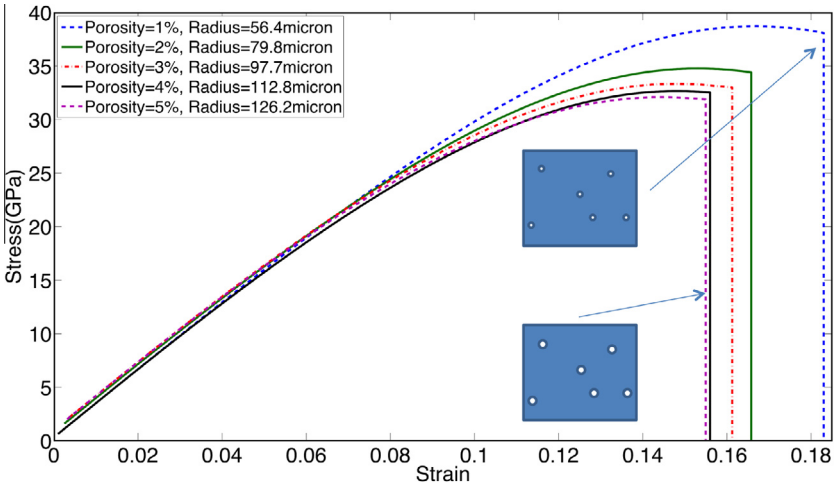

Fig. 8. Uniaxial compressive stress vs. strain at a constant strain rate of 10^6/s, for microstructures with 10^6/m^2 flaw density and an increasing porosity from 1% to 5%.

Table 3
Predicted uniaxial compressive strength for microstructure with flaw density 10^6/m^2, at different strain rates and varying flaw densities.

Porosity (%)	Radius (μm)	Strength (GPa) at various strain rates/percentage increase from strength at strain rate 10^3/s			
		Strain rate = 10^3/s	Strain rate = 10^4/s (%)	Strain rate = 10^5/s (%)	Strain rate = 10^6/s (%)
1	56.4	12.7	13.1/3.1	15.4/21.3	38.7/205
2	79.8	8.1	8.4/3.7	10.5/29.6	34.8/330
3	97.7	6.1	6.4/4.9	8.5/39.3	33.3/446
4	112.8	5.0	5.3/6	7.3/46.0	32.7/554
5	126.2	4.2	4.5/7.1	6.5/54.8	32.1/664

Therefore, the higher crack growth speeds associated with larger pore sizes do not translate to a large decrease in strength because of the high strain rate. At high strain-rates, flaw size is less of a controlling factor than flaw density in determining material strength.

The predicted strengths with varied flaw size are summarized in Table 3 for multiple strain rates. Consistent with the figures, the strength decreases with increasing pore radius at every strain rate, but the decrease is more pronounced at the lower strain rates. The effect of strain rate is greater for larger pores, which see a higher increase in strength with strain rate. At low strain rates the large pores have a significant effect on strength, but at higher strain rates the large pores do not have as significant an effect on strength.

Finally, we consider the case of a fixed porosity of 5%, with both flaw density and flaw size varying accordingly. Low flaw densities will lead to a small number of large pores, and high flaw densities will lead to a large number of small pores, as shown in the microstructure insets in Fig. 9, which shows predicted strength as a function of strain rate. In Fig. 9, we see that at low strain rates, materials with many small flaws are stronger than those with few large flaws. The flaw density is not having an impact on material strength because loading in this range is similar to static loading where, once a crack initiates at a large flaw, the material fails

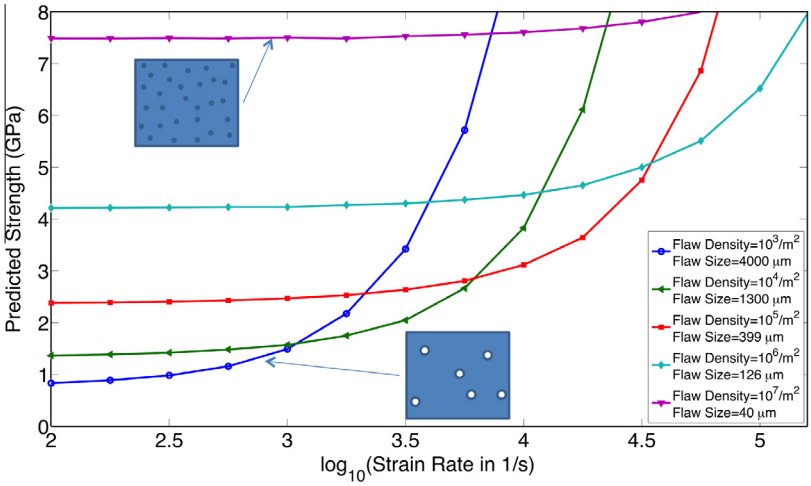

Fig. 9. Compressive strength as a function of strain rate for materials with 5% porosity and varying flaw density and flaw size.

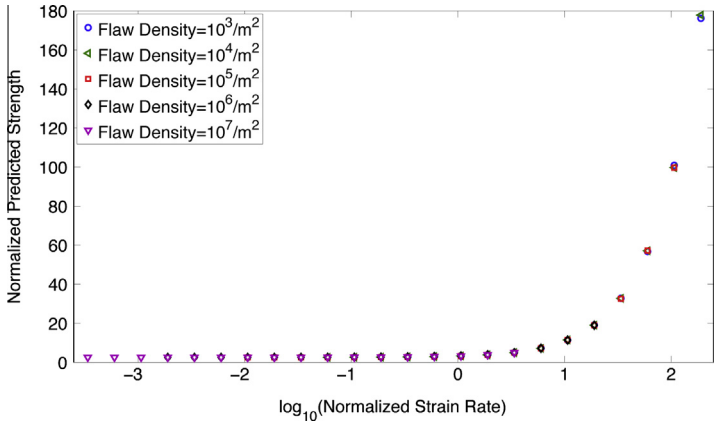

Fig. 10. Normalized predicted strengths vs. normalized strain rate for materials with 5% porosity.

almost immediately. In other words, at low strain rates, flaw size controls. At higher strain rates, the material with a low flaw density ($10^3/m^2$) is the strongest. Although this material has large flaws, the crack growth rate limit is being reached and there are a limited number of flaws to exhibit further crack growth. A larger number of flaws allows more widespread damage related to crack growth; therefore, at high rates flaw density dominates strength.

Kimberley et al. (2013) developed a scaling law that predicts strength of materials with slit-like flaws, based on a characteristic stress σ_o and characteristic strain rate $\dot{\varepsilon}_o$:

$$\sigma_0 = \frac{2.4K_{Ic}}{a\eta^{1/4}} \tag{10}$$

$$\dot{\varepsilon}_0 = \frac{2.4K_{Ic}\eta^{1/4}}{a\sqrt{\rho E}} \tag{11}$$

where a is the average slit flaw size. For materials with pore flaws of uniform radius and porosity ϕ, similar expressions for the characteristic stress and strain rate are:

$$\sigma_0 = \frac{4.25K_{Ic}\eta^{1/4}}{\sqrt{\phi}} \tag{12}$$

$$\dot{\varepsilon}_0 = \frac{4.25K_{Ic}\eta^{3/4}}{\sqrt{\phi\rho E}} \tag{13}$$

The normalized strength σ/σ_0 as a function of the normalized strain rate $\dot{\varepsilon}/\dot{\varepsilon}_0$ are shown in Fig. 10. Scaling the results allows the predicted strength to collapse onto the same curve for any flaw density/flaw size combination.

A few experimental results are available that help confirm the results presented in this section, although there is very little work that directly compares the effects of pore size and number density on high-rate strength. Quasi-static tests on granite specimens with drilled large pores (0.75 to 1.25 mm radius) show that increasing the pore size decreases the material strength at low rates (Wong et al., 2006). In this experiment, small flaws within the material did not activate crack growth, and failure is therefore controlled by large pores. This is confirmed for ceramics by Keleşa et al. (2011), in which they find that the static strength of porous alumina samples is higher in samples with small pores than in samples with the same total porosity but larger pores. Dynamic loading of strain rates up to $3.4 \times 10^3/s$ were performed on porous bronze, a fairly brittle material, in Iqbal et al. (2011). In this work it was found that the strength of samples with lower porosity are more strain-rate sensitive. Since the pores appear to be approximately the same size at the different porosity levels, this suggests that the porosity increase relates to changes in flaw density. These results agree with Table 2, which shows that lower flaw density increases strain rate dependency.

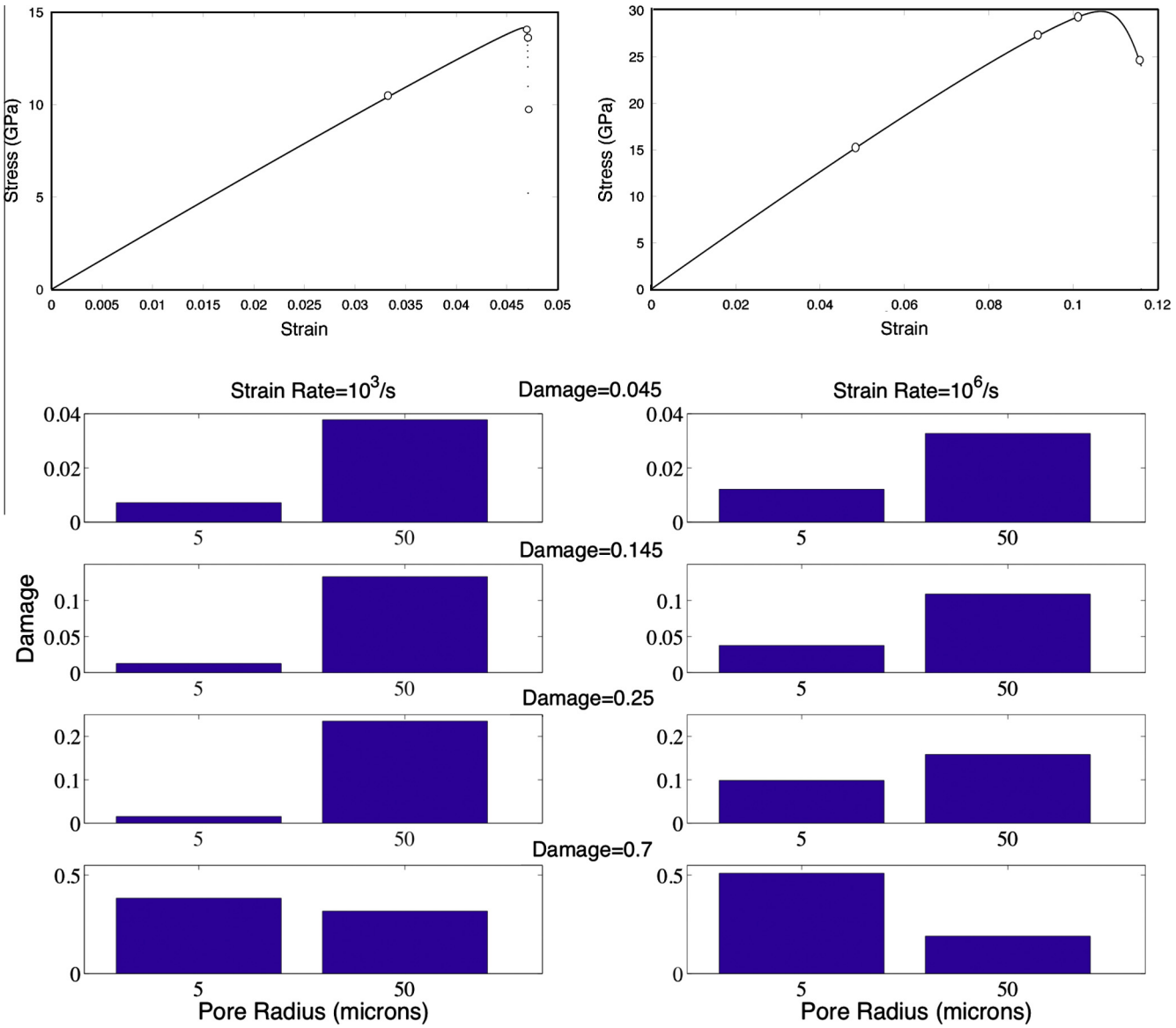

Fig. 11. Plots of damage by flaw radius at various total damage values for bi-valued flaw material loaded at a strain rate of 10^3/s (left) and 10^6/s (right). The corresponding points on the stress–strain curves are shown as white dots in the plots above.

3.2. Bi-valued flaw size distribution

To show how small flaws and large flaws contribute to damage at different strain rates, we create a bi-valued flaw size distribution with 99% 5-micron flaws and 1% 50-micron flaws. The flaw density is set at 10^8 flaws/m^2, which corresponds to a material with 1.56% porosity and an average flaw radius of 5.45 μm. Fig. 11 shows the total damage associated with each flaw size at various points during loading, corresponding to strain rates 10^3/s and 10^6/s. At the lower strain rate the large flaws dominate damage throughout most of the loading, even though only 1% of flaws are large. At the higher strain rate of 10^6/s, the largest flaws activate cracks initially but reach the limiting crack growth speed, allowing the smaller flaws to contribute more to the total damage.

3.3. General flaw size distributions

Real materials contain a distribution of flaw sizes; therefore, we need to consider how flaw size distributions influence material response. For direct comparison, we compare flaw size distributions with the same mean flaw radius of 10 μm and standard deviation of 3.33 μm. In particular, we select the flaw size distributions in Table 4 and plotted in Fig. 12.

The uniform and truncated normal distributions are symmetric about the mean. The gamma distribution is slightly skewed, with the peak of the distribution falling below the mean of 10 μm. The Generalized Pareto distribution has a large number of flaws smaller than the mean and is highly skewed. The inset in Fig. 12 shows the upper tails of the Truncated Normal, Gamma and Generalized Pareto distributions. The uniform distribution terminates at 15.77 μm and, therefore, does not appear on the inset. In order to avoid negative flaw sizes, the truncated normal distribution ends at 0 μm on the lower end, therefore at 20 μm at the upper end in order to maintain symmetry. In theory the Gamma and Generalized Pareto distributions continue to infinity; however, in order for the micromechanical model to be physically reasonable we apply an upper bound of 100 μm to both of these distributions. For the particular parameters chosen for these distributions, the theoretical probability of flaws exceeding this value is extremely small (on the order of 10^{-5} for the Generalized Pareto distribution and

Table 4
Probability Density Functions Defined.

Distribution Type	PDF	Mean	Variance	Parameters
Uniform	$\frac{1}{a_{\max}-a_{\min}}$	$\frac{a_{\max}-a_{\min}}{2}$	$\frac{(a_{\max}-a_{\min})^2}{12}$	a_{min} = 4.23 μm a_{max} = 15.77 μm
Truncated Normal	$\frac{1}{0.9974\sqrt{2\pi\sigma^2}} e^{\frac{-(a-\mu)^2}{2\sigma^2}}$ $\mu-3\sigma \le a \le \mu+3\sigma$	μ	$0.973\ \sigma^2$	μ = 10 μm σ = 3.38 μm
Gamma	$\frac{1}{\beta^2\Gamma(\alpha)} a^{\alpha-1} \exp\left[\frac{a}{\beta}\right]$ $a \ge 0$	$\alpha\beta$	$\alpha\beta^2$	α = 9 β = 1.11 μm
Generalized Pareto	$\frac{1}{\sigma}\left(1+k\frac{a-\theta}{\sigma}\right)^{-1-\frac{1}{k}}$ $a \ge \theta$	$\theta+\frac{\sigma}{1-k}$	$\frac{(\sigma)^2}{(1-k)^2(1-2k)}$	σ = 0.94 μm k = 0.45 θ = 8.60 μm

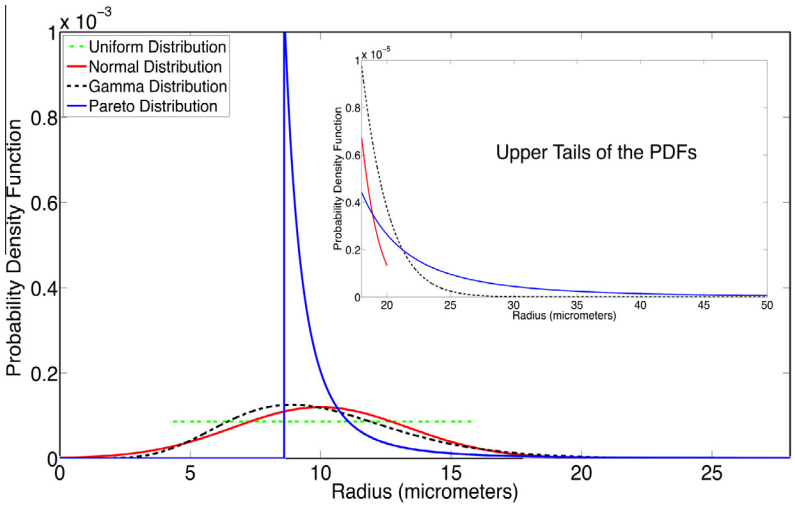

Fig. 12. Probability density functions for flaw size distributions having average flaw radius of 10 μm and standard deviation of 3.33 μm. Inset magnifies the probability density functions in the upper tails.

smaller than 10^{-16} for the Gamma distribution). Note that these exceedance probabilities could be higher with a different set of distribution parameters, which may be the case for various materials. The inset in Fig. 12 shows the gamma distribution decreases rapidly between 20 and 25 μm, whereas the Pareto distribution decreases more gradually. Therefore, the Pareto distribution includes a higher probability of the very largest flaw sizes.

Total porosity is calculated as follows:

$$\phi = \int_0^\infty \eta\pi a^2 g(a)da \approx \sum_i \eta\pi a_i^2 g(a_i)\Delta a \tag{14}$$

Assuming a flaw density η of $10^8/m^2$ with a uniform flaw radius of 10 μm, the total porosity is 3.14%. Assuming a uniform distribution of flaw sizes with the mean equal to 10 μm and a standard deviation of 3.33 μm, the total porosity is 3.49%. Assuming the same mean and standard deviation, the porosity associated with the truncated normal flaw size distribution is 3.49%, the porosity associated with a gamma flaw size distribution is 3.48%, and the porosity associated with a Generalized Pareto flaw size distribution is 3.66%. Because the porosity values vary slightly, we consider two possible sets of flaw population: one in which the flaw density is fixed to $10^8/m^2$ for every distribution, and one in which the flaw density associated with each distribution is adjusted to ensure that the total porosity is 3.14% (i.e., $\eta_{\text{uniform}} = \eta_{\text{gamma}} = 8.997 \times 10^7/m^2$, $\eta_{\text{normal}} = 9.023 \times 10^7/m^2$, $\eta_{\text{Pareto}} = 8.579 \times 10^7/m^2$).

Assuming loading rates of 10^3/s and 10^6/s, the predicted strength for each flaw size distribution is shown in Table 5. In all cases, the uniform flaw size of 10 μm leads to the largest predicted strength. Even though the other distributions have the same mean and variance, they show differences in predicted strength. These results indicate that the full flaw size distribution, not just the mean and variance, is significant to predicting strength. The symmetric distributions predict very similar responses. Skewed distributions like the gamma and Pareto distributions, that include the presence of a small number of large flaws, lead to smaller material strengths in all cases except the strain rate 10^6/s with a fixed porosity level (i.e., with a higher flaw density). At the lower strain rate, the lowest predicted strength comes from the Generalized Pareto flaw size distribution, which is the most heavily skewed. The tail of this distribution decays slowly at very large flaw sizes (see inset in Fig. 12). Although these large flaws have a low probability, they still have a strong effect on the material strength at the lower strain rate. At the higher rate, the strength with a fixed porosity of 3.14% that is predicted from the Generalized Pareto flaw size distribution is slightly higher than the other distributions. This is because the flaw density is reduced more than the other distributions, in order to maintain the constant porosity level. At this higher strain rate, strength is driven more by the number of flaws than by the sizes of the flaws.

To better understand the differences in strength from one distribution to another, we compare the damage contribution by flaw size at failure, under a strain rate of 10^3/s (see Fig. 13). The uniform flaw size distribution shows that damage is skewed toward the larger flaw sizes. This is because the larger flaws activate crack growth more easily, and the density of all flaw sizes is equal. The truncated normal distribution shows a large amount of damage centered just above the

Table 5
Compressive strength, assuming various flaw size distributions.

Flaw size distribution	Strength (GPa), fixed flaw density $\eta = 10^8/m^2$			Strength (GPa), fixed porosity $\phi = 3.14\%$		
	Porosity ϕ (%)	Strain rate = 10^3/s	Strain rate = 10^6/s	η ($10^8/m^2$)	Strain rate = 10^3/s	Strain rate = 10^6/s
Uniform flaw size = 10 μm	3.14	18.4	21.3	1	18.4	21.3
Uniform PDF	3.49	15.8	19.2	0.8997	16.9	20.2
Truncated Normal PDF	3.49	15.8	19.3	0.8997	16.8	20.3
Gamma PDF	3.48	15.6	19.2	0.9023	16.6	20.2
Generalized Pareto PDF	3.66	13.0	19.0	0.8579	13.2	20.5

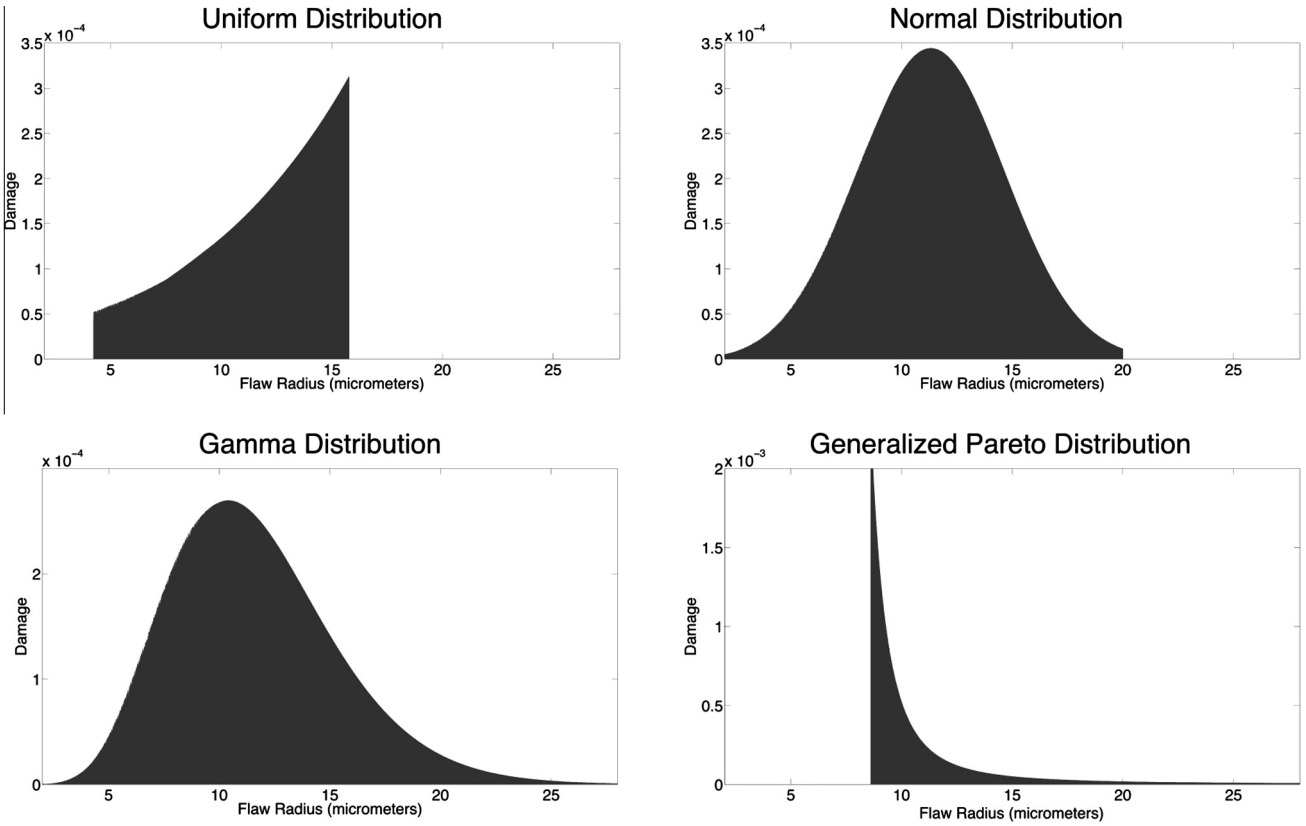

Fig. 13. For a strain rate of 10^3/s, the resulting contribution to damage by flaw size at material failure (total damage = 0.7) is shown for each of the four flaw size distributions.

mean flaw size because that is where the most significant combination of larger flaw density and significant crack growth due to large size is found. The gamma distribution of flaw size is skewed to a higher density of small flaws, but similar to the truncated normal distribution the peak damage contribution is still slightly above the mean flaw size. The Pareto distribution activates crack growth from the full range of flaw sizes within the distribution. Both the large number of small flaws and the small number of large flaws contribute to total damage. Even though the damage associated with any single flaw size larger than 20 μm is relatively small, the cumulative damage from all flaws larger than 20 μm (twice the mean) is 13% of the total damage. Because the truncated symmetric distributions do not contain any flaws larger than 20 μm, the total damage in these cases grows less quickly than the total damage associated with the Generalized Pareto distribution. Therefore, the symmetric, bounded distributions predict more slowly growing damage and higher strength.

3.4. Effect of setting a lower threshold on flaw size

Experimental observations that attempt to quantify pore size distributions are limited by the resolution of the technique used to resolve these pores. Looking at Fig. 13, the damage associated with very small flaws (e.g., less than half the mean, or 5 μm) is very small. Therefore, we would expect that there exists a lower threshold on flaw sizes required to accurately predict strength. This lower threshold is useful to identify which, if any, deficiencies of the experimental characterizations must be addressed.

This parameter study assumes a flaw population with a mean pore radius of 14.5 μm, porosity 4% and a very small minimum pore radius of 0.2 μm. The Generalized Pareto distribution (see Table 4) has been observed to be a reasonable representation of flaw size in real materials (Bakas et al., 2012). In order to match the desired mean, minimum and porosity, we modify the Generalized Pareto distribution as follows:

$$g(a) = \begin{cases} \frac{\frac{1}{\sigma}\left(1-k\frac{a-\theta}{\sigma}\right)^{-1-\frac{1}{k}}}{1-\left(1+k\left(\frac{0.2-\theta}{\sigma}\right)\right)^{-\frac{1}{k}}}; & a \geqslant 0.2 \\ 0; & \text{otherwise} \end{cases} \tag{15}$$

with the Pareto shape parameter k equal to 5, the scale parameter σ equal to 10^{-3} μm, and the threshold of the underlying distribution equal to -10^{-3} μm. Note that this function consists of the Generalized Pareto PDF in the numerator, normalized by the Generalized

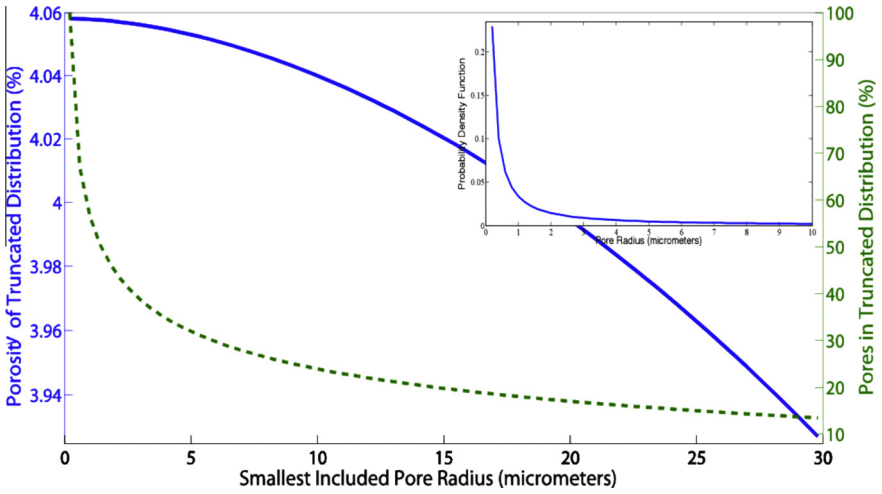

Fig. 14. Change in porosity and number of pore flaws by minimum flaw size for 14.5 μm mean distribution. The inset shows the flaw size distribution function.

Pareto cumulative density function in the denominator, evaluated at a pore radius of 0.2 μm. The lower threshold of this modified GP distribution (shown in the inset of Fig. 14) is therefore 0.2 μm.

To study the effect of setting a lower threshold on pore size that is greater than the actual lower threshold of 0.2 μm, we truncate the probability density function by setting a minimum flaw size $a_{\min}$:

$$g^T(a) = \left\{ \begin{array}{ll} \frac{g(a)}{\int_{a_{\min}}^{200} g(a)da}; & a_{\min} \leqslant a \leqslant 200 \\ 0; & \text{otherwise} \end{array} \right\} \tag{16}$$

where $g^T(a)$ is the truncated probability density function. Normalizing by the denominator ensures that the integral of the truncated probability density function $g^T(a)$ is unity. We also define a truncated pore flaw density, based on the fraction of flaws that are ignored by the truncated distribution:

$$\eta^T = \eta\left(1 - \int_{0.2}^{a_{\min}} g(a)da\right) \tag{17}$$

where η^T is the pore flaw density of the truncated distribution, and η is the original flaw density.

Fig. 14 shows the flaw density and porosity as a function of the threshold $a_{\min}$. The change in porosity with truncation of the distribution is relatively small, because we are neglecting extremely small pores that do not contribute greatly to porosity. However, the change in flaw density is more significant because we are removing a relatively large number of pores from the population. The truncated flaw size distribution and flaw density are input to the micromechanics model for a range of threshold values $a_{\min}$. Fig. 15 shows the percent increase in predicted strength as a function of $a_{\min}$, for three loading rates.

At very small lower thresholds, there is no change in strength because these flaws do not exhibit significant crack growth at any of these strain rates. With larger thresholds, the significance of excluding small flaws increases. The change in strength is larger for the higher strain rate loading, which activates more of the small flaws and exhibits a greater effect from ignoring those flaws. At moderate strain rates, the change in predicted strength compared to the full flaw size distribution is small even at the minimum flaw size of 30 μm (over two times the mean flaw size of 14.5 μm corresponding to the original pore size distribution).

4. Discussion of predicted vs. actual material strength

In general, the dynamic strengths shown in the numerical example are an overprediction relative to the actual material strength for AlN. It is important to emphasize that the goal of this paper is not to capture quantitatively an experimentally obtained

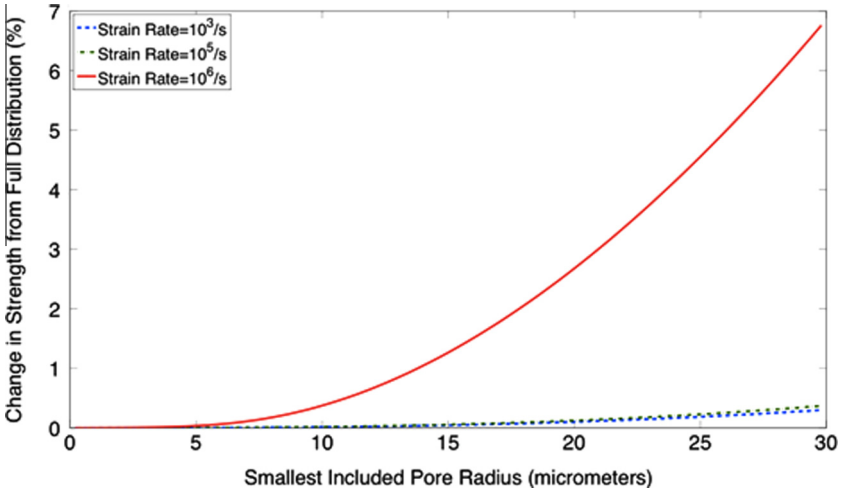

Fig. 15. Change in strength with varying minimum flaw size for the modified Pareto flaw size distribution with a mean radius of 14.5 μm.

Table 6
Compressive strength at varying strain rates, based on a flaw population that consists of circular flaws from a Pareto distribution with total porosity 3.66% and slit flaws of uniform half size 3 μm and number density $7 \times 10^9/m^2$.

Strain rate	Strength (GPa)		
	Circular flaws only	Slit flaws only	Both flaws
10^3/s	13.0	9.29	8.20
10^4/s	13.0	9.32	8.46
10^5/s	14.8	9.39	8.68
10^6/s	19.0	9.66	9.04

dynamic strength of a specific material; however, some discussion of the error in the model predictions is merited. Generally, the error in the predicted strength is attributed to a number of factors:

(1) *Input parameters that represent the initial flaw population and/or the material properties are not known and therefore may not be realistic for AlN*: Except for total porosity and possibly the general power-law shape of the distribution describing pore sizes, other distribution parameters such as the mean, variance and skewness are not well understood. Also, the actual effective porosity may be higher than that assumed here because of the presence of weak inclusions that do not affect experimental measures of porosity but that significantly affect material strength. Finally, the model only addresses pre-existing flaws and does not incorporate pores that may activate and grow under loading. Improved characterizations of these pore populations would be of significant value in future work. Some of the other material parameters used in the model are also not well understood. For example, the friction coefficient at crack interfaces has not been measured; if the actual coefficient is less than the assumed value of $\mu = 0.4$ then the predicted strength would decrease. Similarly, some basic bounds on the crack growth parameters α and γ are available in the literature for other brittle materials, but they are not known for AlN.

(2) *The model addresses only circular flaws*: The pre-existing flaw population in AlN could consist of both pore-like and slit-like flaws. In order to demonstrate this, the current model is adapted to include both circular and slit-like flaws by incorporating the Paliwal and Ramesh model (2008). Assuming that the slit-like flaws are associated with grain boundaries, then we add a slit flaw population that relates to the grain size in the material. For example, a typical grain diameter in AlN is 6 μm and assuming that 20% of grain boundaries manifest themselves as slit-like flaws, then the slit flaw population is $7 \times 10^9/m^2$ flaws of half-size 3 μm. Using the Generalized Pareto distribution of circular flaws with number density $10^8/m^2$ (porosity 3.66%) described in Section 3.3, Table 6 shows the predicted strength as a function of strain rate. While these values remain higher than experimentally observed strength in AlN, this illustrates how different flaw types work together to reduce the predicted strength.
Other flaw families are not included in this model, such as large irregular disc-shaped carbonaceous inclusions that have been observed in many ceramics. These would manifest as large slit-like flaws in the model. Pre-existing cracks associated with thermal stresses developed during processing may result in additional slit-like flaws. These flaws are not addressed here because little or no quantitative information about them is available. If they were added to the flaw population in this study, the predicted strength would decrease.

(3) *The model does not address crack coalescence*: As cracks grow from pre-existing flaws, they will eventually intersect cracks associated with other flaws. This crack coalescence is not considered in the model, although it might contribute to a higher damage rate and therefore a lower predicted strength. This is an interesting direction for future work.

(4) *The model is two-dimensional*: The micromechanical model is developed in a two-dimensional plane strain context, although of course the material itself is three-dimensional. Also, it is not clear how one connects an observed three-dimensional flaw population to a two-dimensional flaw population. This assumption affects the results, although it is not clear whether the effect is to increase or decrease the predicted strength.

(5) *The model does not include any inelastic mechanisms that may be associated with failure*: Other failure mechanisms, such as inelasticity, amorphization, and shear bands may play a role in AlN, although this remains a very active area of discussion in ceramics. The effect of these mechanisms is small relative to the crack-related damage considered here, but these mechanisms may serve to further suppress dynamic strength of AlN.

Addressing these parameters through more complete experimental characterization may provide a more realistic strength in particular for AlN, but this is not the specific goal of this paper. Instead, the focus of this paper is to propose a model that allows a basic understanding of how pore population characteristics in a brittle material affect compressive dynamic strength.

5. Conclusions

This paper presents a method to analyze the compressive dynamic strength of brittle materials with a distribution of initial circular flaws. The model follows the framework of Paliwal and Ramesh (2008), but with a modified pore flaw model as opposed to a slit-like flaw model. We modify the original two-dimensional circular pore stress intensity suggested by Sammis and Ashby (1986), by adding a term to the stress intensity that accounts for small initial inclined cracks. Analyzing the expression for the Mode I stress intensity, we find a theoretically-based justification for assuming an initial 'pop-in' crack length of 15% of the pore radius, which agrees well with the experimental observations of Sammis and Ashby (1986).

The model is able to capture the relative effects of changes to the initial flaw population, summarized as follows:

- Predicted strength decreases with increased pore radius, increased flaw density, and/or increased porosity.
- Strain-rate-effects are more significant in materials with large flaw sizes, because larger flaw sizes significantly reduce strength at low rates but not at high rates. Similarly strain-rate effects are more significant in materials with lower flaw density.
- In order to increase dynamic strength at low to moderate strain rates, it is most effective to control the presence of large pores. However, in order to increase dynamic strength at high strain rates, it is more effective to control the total number of pores, regardless of size.
- Assuming a single uniform flaw size equal to the average flaw size is not conservative for dynamic strength prediction. The strength predicted using a Pareto distribution with the same mean is significantly lower than the strength assuming a uniform flaw size.

- Truncating flaws up to 2–3 times the mean flaw size had minimal effect on predicted dynamic strength at strain rates up to 10^5/s. Truncating flaws up to the mean flaw size had minimal effect on predicted dynamic strength at a strain rate of 10^6/s. These results suggest that we can identify a reasonable resolution level below which experimental characterization of flaws is not necessary.

In future efforts, we would like to consider extending the model to incorporate more of the mechanisms that drive dynamic failure, including the following:

- A combined pore/slit flaw model was used in the discussion section to demonstrate how both flaw populations reduce strength for this particular example. However, there is not a full parametric study to identify the relative effects of both flaw populations.
- This model addresses indirect crack interaction through a self-consistent model that relates global damage to local stresses exerted on individual flaws. Explicit crack interaction in the form of crack coalescence is not considered in the current model.
- The crack growth rate parameters α and γ are not well understood and are set equal to one here. These values can be adjusted if new experiments provide better-informed parameters.
- Pores/weak inclusions were idealized as circular voids with initial cracks. These could also be modeled as ellipsoidal or irregular shaped voids that are inclined relative to the loading direction.
- Poisson's ratio is assumed to remain constant, but in an anisotropic medium we would expect that the two Poisson's ratios ν_{12} and ν_{21} would differ. The effect of damage on these parameters merits further study.
- The initial flaw population is assumed to be constant. However, additional voids may activate and grow during loading and increase the flaw population with damage.
- This model does not explicitly consider plasticity and dislocation effects near the crack tips, which may have an effect on the fracture behavior.
- We assume that pores remain circular. However, pore collapse may occur at high stress levels and then pores may act similarly to slit flaws.

Acknowledgements

This material is based on work supported by the National Science Foundation under Grants Nos. 0969972 and 0801471, and through a Cooperative Agreement between the Materials in Extreme Dynamic Environments (MEDE) Consortium and US Army Research Lab (Contract number W911NF-12-2-0022). Any opinions, findings, and conclusions or recommendations expressed in this paper are those of the authors and do not necessarily reflect the views of the National Science Foundation or the Army Research Lab.

References

Budiansky, B., O'Connell, R., 1976. Elastic moduli of a cracked solid. International Journal of Solids and Structures 12 (2), 81–97.
Horii, H., Nemat-Nasser, S., 1986. Brittle failure in compression: splitting, faulting, and brittle ductile transition. Philosophical Transactions of the Royal Society of London A 319, 337–374.
Ravichandran, G., Subhash, T., 1995. A micromechanical model for high strain rate behavior of ceramics. International Journal of Solids and Structures 32 (17–18), 2627–2646.
Huang, C., Subhash, G., Vitton, S., 2002. A dynamic damage growth model for uniaxial compressive response of rock aggregates. Mechanics of Materials 34 (5), 267–277.
Deshpande, V., Evans, A., 2008. Inelastic deformation and energy dissipation in ceramics: a mechanism-based constitutive model. Journal of the Mechanics and Physics of Solids 56 (10), 3077–3100.
Paliwal, B., Ramesh, K., 2008. An interacting micro-crack damage model for failure of brittle materials under compression. Journal of the Mechanics and Physics of Solids 56 (3), 896–923.
Sammis, C., Ashby, M., 1986. The failure of brittle porous solids under compressive stress states. Acta Metallurgica 34 (3), 511–526.
Sih, G., 1973. Handbook of Stress-Intensity Factors. Lehigh University Institute of Fracture & Solid Mechanics, Lehigh.
Hu, G., 2012. The Failure of Brittle Materials under Dynamic Multiaxial Loading (Ph.D. Dissertation). Johns Hopkins University, Mechanical Engineering, Baltimore
Kimberley, J., Ramesh, K., Daphalapurkar, N., 2013. A scaling law for the dynamic strength of brittle solids. Acta Materialia 61 (9), 3509–3521.
Wong, R., Lin, P., Tang, C., 2006. Experimental and numerical study on splitting failure of brittle solids containing single pore under uniaxial compression. Mechanics of Materials 38 (1–2), 142–159.
Keleşa, Ö., García, R.E., Bowman, R.E., 2011. Stochastic failure of isotropic, brittle materials with uniform porosity. Acta Materialia 61 (8), 2853–2862.
Iqbal, N., Xue, P., Liao, H., Wang, B., Li, Y., 2011. Material characterization of porous bronze at high strain rates. Materials Science and Engineering A 528 (13–14), 4408–4412.
Bakas, M., McCauley, J., Greenhut, V., Niesz, D., Haber, R., West, B., 2012. Quantitative analysis of inclusion distributions in hot pressed silicon carbide. International Journal of Impact Engineering 50, 40–48.